DOI: 10.1002/zaac.201200517

On the Control Parameters of the Quasi-One Dimensional Superconductivity in Sc_3CoC_4

Georg Eickerling,*[a] Christoph Hauf,[a] Ernst-Wilhelm Scheidt,[a] Lena Reichardt,[a] Christian Schneider,[a] Alfonso Muñoz,[b] Sinhué Lopez-Moreno,[c] Aldo Humberto Romero,[d,e] Florence Porcher,[f] Gilles André,[f] Rainer Pöttgen,[g] and Wolfgang Scherer*[a]

Keywords: Transition-metal carbides; Low dimensional; Superconductors; Electron density; Phonon dispersion

Abstract. Within the series of ternary rare-earth transition metal carbides Sc_3TC_4 (T = Fe, Co, Ni) only the Co congener displays a structural phase transition at 72 K and an onset of bulk superconductivity at 4.5 K. In this paper we present the results of a detailed analysis of the structural, electronic, and vibrational properties of the low-temperature phase of Sc_3CoC_4 that represents one of the few well-documented examples of a quasi one-dimensional (1D) superconductor. Variable temperature neutron powder diffraction and low temperature X-ray diffraction experiments were performed in order to confirm the subtle structural distortions during the phase transition. The results of periodic electronic structure calculations indicate, that the structural transition can clearly be identified as a Peierls-type distortion and by a comparison with the isostructural carbide Sc_3FeC_4 we are able to identify the chemical, electronic, and the vibrational control parameters of the transition. Topological analyses of the electron density distribution and of the valence shell charge concentrations at the cobalt atom finally allow us to directly correlate the changes in the electronic structure due to the Peierls transition in reciprocal space with the according subtle changes in the real space properties of Sc_3CoC_4.

Introduction

The ternary rare-earth transition metal carbides $RE_xT_yC_z$ represent a class of compounds featuring a wide range of interesting structural, chemical, and physical properties.[1] YCoC for example is composed of linear Co–C chains,[2] whereas the Sc_3TC_4 (T = Fe, Co, Ni, Rh, Ir, Ru, Os) carbides are formed by quasi one-dimensional [$T(C_2)_2$] ribbons. In both cases, these structural motives are embedded in a matrix of *RE* atoms. In previous studies we have investigated the physical and electronic properties of the isostructural compounds Sc_3TC_4 [T = Fe (**1**), Co (**2**) and Ni (**3**)] by means of experimental charge density studies and low-temperature resistivity, specific-heat and susceptibility measurements.[3,4] Even though the electron count of the compounds can be varied in a wide range, it is only Sc_3CoC_4, for which bulk superconductivity can be observed at temperatures below T_c = 4.5 K.[4] Therefore, this compound can serve as one of the rare model systems for a quasi one-dimensional (1D) superconductor[5] and has recently been identified as one of the "most characteristic 1D superconductors" known to date.[6] The structural phase transition observed at 72 K for Sc_3CoC_4 but not for the Fe and Ni congeners seems to play a major role for the onset of superconductivity in the compound. In the presented work we will focus on the structural and electronic properties of the low-temperature phase of Sc_3CoC_4 (LT-**2**). We therefore re-investigated the low temperature structure of **2** by variable-temperature neutron powder and single-crystal X-ray diffraction experiments and performed electronic structure calculations as well as a topological analysis of the electron density. The latter can only be based on DFT calculations as experimental charge density studies of the low-temperature structure are prevented by the systematic twinning induced by the *translationengleiche* phase transition.

* Dr. G. Eickerling
Fax: +49-821-598 3327
E-Mail: georg.eickerling@physik.uni-augsburg.de
* Prof. Dr. W. Scherer
E-Mail: wolfgang.scherer@physik.uni-augsburg.de
[a] Institut für Physik
Universität Augsburg
Universitätstrasse 1
86179 Augsburg, Germany
[b] Departamento de Física Fundamental II,
Instituto de Materiales y Nanotecnología
Universidad de La Laguna,
Tenerife, Spain
[c] Escuela Superior Cd. Sahagún
Universidad Autónoma del Estado de Hidalgo
Carretera Cd. Sahagún-Otumba s/n. 43990, Hidalgo, México
[d] Physics Department
West Virginia University
Morgantown, West Virginia 26506–6315 USA
[e] Max Planck Institut für Mikrostruktur Physik
Weinberg 2
06120 Halle, Germany
[f] Laboratoire Léon Brillouin
UMR12 CEA-CNRS
Bât 563 CEA Saclay
91191 Gif sur Yvette Cedex, France
[g] Institut für Anorganische und Analytische Chemie
Universität Münster
Corrensstrasse 30, 48149 Münster, Germany
Supporting information for this article is available on the WWW under **http://dx.doi.org/10.1002/zaac.201200517** or from the author.

Special Issue

In the widely applied BCS-Theory, the superconducting properties of a compound, especially the temperature of the respective transition T_c, depend mainly on three parameters: (*i*) the density of states at the Fermi-level $N(E_F)$, (*ii*) the phonon frequencies ω, and (*iii*) the electron-phonon coupling parameter *V*.[7] In order to understand the superconducting properties of the LT-phase of **2** we aimed at a systematic study of these control parameters. We therefore synthesized the solid solutions $Sc_3Co_{1-x}Ni_xC_4$ and $Sc_3Co_{1-x}FeC_4$, in which we can systematically vary the electron count and, in combination with electronic structure calculations on LT-**2**, can study the effect of the varying electron count on the electronic and physical properties of **2**. In a second step, we will present results of lattice-dynamic calculations on the high- and low temperature phase of Sc_3CoC_4 in order to elucidate the vibrational properties of the superconducting phase.

The presented work is therefore organized as follows: First we focus on the LT-structural properties of **2** and next the vibrational and electronic properties of the LT-phase of **2** will be analyzed in detail. Finally we will discuss the structural and physical properties of the solid solution $Sc_3Co_{1-x}(Ni/Fe)_xC_4$.

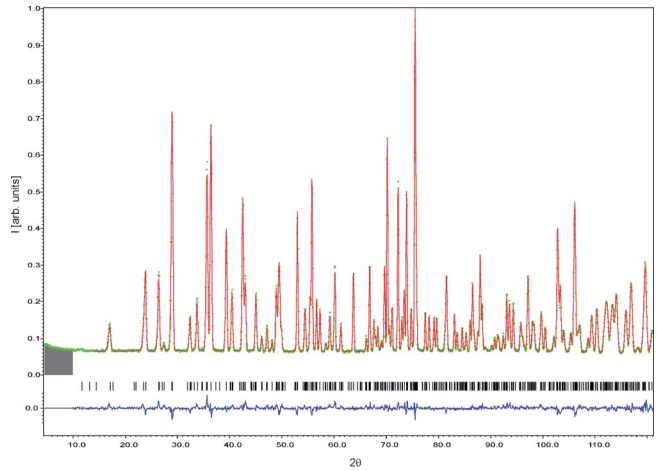

Figure 1. Neutron powder diffraction pattern (10 K) (green crosses) including the Rietveld profile (red line), the Bragg reflection positions (vertical black lines) and the profile difference (blue line) of LT-**2**. The final Rietveld fit was obtained from a combined single-crystal X-ray/neutron powder diffraction refinement. The data in the grey shaded area ($4.5° < 2\theta < 9.5°$) was excluded from the refinement.

Results and Discussion

We start our discussion by presenting the results of a variable temperature neutron powder diffraction study on the LT structure of **2**. The structural phase transition observed for Sc_3CoC_4 can be characterized as a *translationsgleiche* transition of index *t*2 followed by an isomorphic transition of index *i*2.[4] This leads to a symmetry reduction from the original orthorhombic space group *Immm* to the monoclinic space group *C*2/*m*, which is accompanied by a pseudo-merohedral twinning of the crystal.[1,8] In order to verify the structural parameters and the transition temperature T_s of 72 K reported in an earlier study,[4] we reinvestigated the LT-phase structure of **2** by low-temperature neutron powder diffraction and high-resolution single-crystal X-ray diffraction experiments (see Figure 1). The resulting structural parameters are listed in Table 1, which for comparison also contains the structural data from the previous X-ray diffraction study and the according parameters of the high-temperature phase of **2** (HT-**2**). The variable temperature neutron diffraction experiments show the structural transition to take place at 72 K (see S3, Supporting Information), confirming the transition temperature reported earlier based on specific heat measurements.[1,4]

Table 1. Salient structural parameters /Å,° of the HT- and LT-phase of **2** obtained from X-ray and combined X-ray/neutron (XN) diffraction experiments at room temperature and 9 K, respectively.

	HT[a)]	LT[b)]	X-ray	XN
a	3.3935(10)	5.5375(6)	5.5183(13)	5.5320(4)
b	4.3687(10)	12.030(2)	11.9893(29)	12.0109(2)
c	11.9851(10)	5.5368(5)	5.5206(13)	5.5322(4)
β	90	104.77(1)	104.66(1)	104.805(1)
Co–C	2.0886(4)	2.097(3)	2.0979(4)	2.0986(1)
		2.109(3)	2.1073(4)	2.1069(1)
C–C	1.4539(8)	1.455(8)	1.4356(3)	1.4506(1)
Co–Co	3.3935(10)	3.1588(11)	3.1529(5)	3.1556(1)
		3.6005(11)	3.5932(6)	3.5948(2)

a) Ref. [3]. b) Ref. [4].

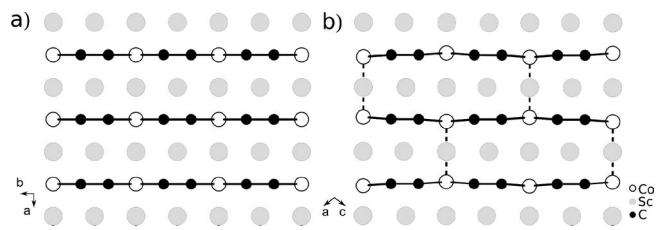

Scheme 1. Ball-and-stick representation of (a) the HT- and (b) the LT-structure of **2**. The short Co–Co contacts resulting from the structural phase transition are indicated by dashed lines for LT-**2** in (b).

The main structural change (Scheme 1) due to the phase transition is the out-of-plane displacement of the cobalt atoms with respect to their original positions in the plane of the $[T(C_2)_2]$ ribbons (HT modification).

This distortion results in the formation of Co···Co pairs with alternating shortened [*d*(Co···Co) = 3.1556(1) Å] and elongated [*d*(Co···Co) = 3.5948(2) Å] distances with respect to the equidistant Co chains [*d*(Co···Co) = 3.3935(10) Å] in the HT modification. Accordingly, the Co displacements occur along the crystallographic *a* axis of the HT phase perpendicular to the $[T(C_2)_2]$ ribbons (dashed lines in Scheme 1). The rather strong and covalent C–C bond lengths are hardly affected by the distortion of the Co coordination environment, solely the Co–C bonds become slightly elongated. The overall agreement between structural data obtained from the previous X-ray and the recent X-ray/neutron data is very good. However, significantly lower *e.s.d.*s were obtained by the combined single-crystal X-ray and neutron powder diffraction study since the latter experiment is not biased by the systematic twinning of the single crystals during the transition into the LT phase.

Zeitschrift für anorganische und allgemeine Chemie ZAAC Journal of Inorganic and General Chemistry

The Topology of the Electron Density

In previous studies we have analysed the bonding situation within the $[T(C_2)_2]$ ribbons and between the $(C)_2$ units and the scandium matrix in HT-**2**.[3] With respect to these interactions we emphasize the high degree of experimental reproducibility of the according topological parameters. In Table 2 and Table S9 (Supporting Information) we compare results obtained from measurements of **2** on an Ag micro-focus/CCD-detector setup (exp. 2, this study) with the according results reported earlier, where a standard Mo sealed-tube/scintillation counter detector setup (exp. 1) was employed (for details, see the Experimental Section and Table S9, Supporting Information).[3]An excellent agreement is observed between both experiments, even for the subtle features of the rather flat electron density distribution in the Sc–$(C)_2$ bonding region.

Table 2. Salient experimental and theoretical topological parameters of the HT- and LT-phase of **2**. The calculated values are based on the relaxed geometries of HT-**2** and LT-**2**. Experimental data (exp. 1) for comparison with exp. 2 (this study) was taken from Ref. [3]. For details on exp. 2 see the experimental section.

			$\rho(\mathbf{r})$ /e·Å^{-3}	$\nabla^2\rho(\mathbf{r})$ /e·Å^{-5}	ε
HT	Co–C	theor.	0.562	4.143	0.01
		exp. 1[a)]	0.581	5.4	0.17
		exp. 2	0.534	5.2	0.41
	C–C	theor.	1.765	–17.775	0.00
		exp. 1[a)]	1.813	–12.0	0.09
		exp. 2	1.845	–8.7	0.20
	Co–Co	theor.	0.148	0.393	0.12
		exp. 1[a)]	0.125	0.355	8.17
		exp. 2	0.124	0.351	0.46
LT	Co–C		0.566	4.140	0.04
			0.550	4.052	0.04
	C–C		1.777	–18.113	0.00
			1.779	–18.136	0.00
	Co–Co		0.127	0.342	0.29
			0.177	0.387	0.28

a) Ref. [3].

In the following, we will concentrate on the changes of the electronic structure induced by the structural phase transition of **2** (Table 2). In the HT phase of **1** and **2** one finds one *T*–*T* bond critical point [Co–Co: $\rho(\mathbf{r}_c)$ = 0.124/0.148 e·Å^{-3}, $\nabla^2\rho(\mathbf{r}_c)$ = 0.351/0.393 e·Å^{-5}; Fe–Fe: $\rho(\mathbf{r}_c)$ = 0.113/0.160 e·Å^{-3}, $\nabla^2\rho(\mathbf{r}_c)$ = 0.371/0.296 e·Å^{-5}; experimental (exp. 2 Ref. [3])/calculated values, respectively] hinting for a potential chemical interaction between *T* atoms of neighboring quasi one-dimensional $[Co(C_2)_2]$ ribbons at high temperatures. In accordance with the two different Co–Co bond lengths, two different Co–Co BCPs [$\rho(\mathbf{r}_c)$ = 0.127, $\nabla^2\rho(\mathbf{r}_c)$ = 0.342 e·Å^{-5} and $\rho(\mathbf{r}_c)$ = 0.177 e·Å^{-3}, $\nabla^2\rho(\mathbf{r}_c)$ = 0.387 e·Å^{-5}, calculated values] are observed in LT-**2** indicating an alternating strengthening and weakening of the respective Co–Co contacts. All other topological parameters appear to be rather unaffected by the phase transition, in accordance with the respective structural parameters. However, a more sensitive measure of subtle electronic changes is provided by the polarization pattern of the negative Laplacian, $L(\mathbf{r}) = -\nabla^2\rho(\mathbf{r})$, in the valence region of the cobalt atoms. It has been demonstrated by *Bader* et al. that the sign of $L(\mathbf{r})$ indicates where charge density is locally concentrated [$L(\mathbf{r}) > 0$] or locally depleted [$L(\mathbf{r}) < 0$].[9,10] The $L(\mathbf{r})$ function can in addition be employed to resolve the shell structure of atoms,[11,12] even though the fourth, fifth, and sixth shell for elements of periods 4–6, respectively, is not revealed as positive maxima in $L(\mathbf{r})$.[13–16] *Bader* et al. suggested as a convention that the outermost shell of charge concentration (CC) of an atom (i.e. the third shell of CC of the iron and cobalt atom) represents its (effective) valence shell charge concentration (VSCC).[17,18] In the presence of ligands, this VSCC of transition metal atoms displays a fine structure, the so called *atomic graph*. As demonstrated in earlier publications, it is the atomic graphs of the *T* atoms, which allows for the discrimination of the isostructural systems Sc_3TC_4 with *T* = Fe, Co and Ni.[1,3,4]

For the HT phase of **2** four strong local charge concentrations and depletions in the $[T(C_2)_2]$ ribbon plane in combination with two shallow zones of local charge depletion (CD) in the direction of the Co···Co chains are observed in the experimental (Figure 2a and b for exp. 1 and exp. 2, respectively) as well as in the calculated electron density distributions (Figure 2c). We note again the excellent reproducibility of the re-

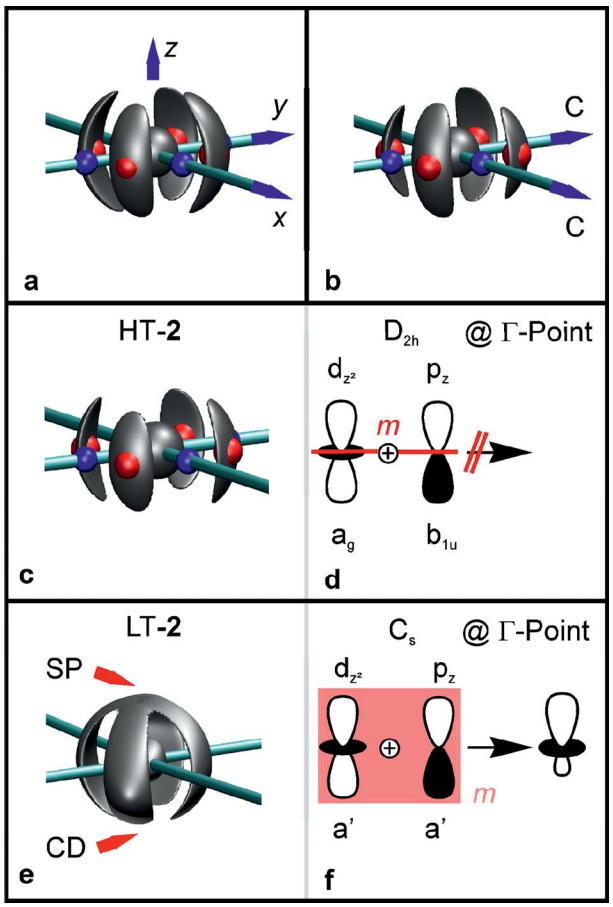

Figure 2. Experimental ((a) exp. 1,(b) exp. 2) and calculated (c, e) $L(\mathbf{r})$ envelope maps of (a–c) HT-**2** and (e) LT-2; $L(\mathbf{r})$ = 1100 (a–c) and 940 (e) e·Å^{-5}, respectively. Red and blue spheres indicate the position of local CCs and CDs, respectively; (d, f) Schematic sketches illustrating the formation of the *p*/*d* hybrid orbitals, which leads to the observed asymmetry in the polarization pattern in the VSCC of Co in LT-**2**.

Special Issue

sults between two different experimental setups observed not only for the topological parameters of the electron density in the bonding regions (vide supra) but also for the more sensitive atomic graphs observed in the VSCC of the cobalt atom. Due to the local D_{2h} symmetry of the coordination environment of the cobalt atoms, the CCs located in the direction of the ribbons can be discriminated from those located perpendicular to it (1451 [1425] versus 1432 [1422] e•Å^{-5}). On the other hand, the shallow CD zones observed above and below the ribbon plane are equal due to symmetry restrictions (966 [954] e•Å^{-5}; exp.2, calculated values in square brackets). This is different for the LT phase, where an asymmetry of the CD zone above and below the ribbon plane is observed (see Figure 2e). Interestingly, it is the CD zone located in the direction of the long Co–Co contact, which is more depleted [858 e•Å^{-5}], while the one pointing in the direction of the short Co–Co contact is significantly less depleted [945 e•Å^{-5}] compared to HT-**2**. This asymmetry in the polarization pattern perpendicular to the ribbon-direction might hint for an increased contribution of Co *p*-type orbitals in LT-**2** (vide infra) causing a polarization of the Co–Co bonding density.

The Electronic Structure

In this section we will link real and reciprocal space properties by correlating electronic features observed in the charge density and its Laplacian distributions with those observed in the band structure of HT-**2** and LT-**2**. We first analyse the change of the density of states (DOS) at the Fermi-level $N(E_F)$ during the HT → LT phase transition of **2**. We find a significant reduction of the DOS at the Fermi-level by almost 25% [$N(E_F)$ = 3.52 and 2.67 states/eV for the HT- and the LT-phase, respectively] which is somewhat surprising in the light of the observed onset of bulk superconductivity in LT-2 below 4.5 K.

Analysing the changes in the electronic structure in more detail by considering the site- and state projected DOS (pDOS, see Figure 3), the observed reduction of $N(E_F)$ is revealed to be mainly due to the changes of the DOS of the pseudo-degenerate $d_{xz/yz}$ and the d_{z^2} orbitals of cobalt, which are the dominating states contributed by the Co atom to $N(E_F)$. We note, that throughout this study a rotated reference coordinate system was employed, which is obtained by a rotation of 45° with respect to the crystallographic axes and a permutation such that the *z* axis is orientated perpendicular to the [Co(C$_2$)$_2$] ribbon plane (for details see the Supporting Information and Ref. [3]). The splitting of the d_{z^2} and the $d_{xz/yz}$ type states into filled and empty states can clearly be identified as origin of the decreasing N(E_F) in LT-**2**. We note, however, that the pseudo-degeneracy of the $d_{xz/yz}$ orbitals remains intact in the filled and empty states after and during the HT → LT phase transition. This is remarkable since the transition is connected with a significant reduction of the local site symmetry at the cobalt atoms (D_{2h} → C_s). A lifting of the $d_{xz/yz}$ degeneracy would have been a clear evidence for a Jahn-Teller (JT) type distortion mechanism as driving force for the structural phase transition.[19] Accordingly, the still existent pseudo degeneracy of the $d_{xz/yz}$ orbitals in LT-**2** suggests that the true driving force might be of different nature. Indeed, the splitting of the $d_{xz/yz}$ states at E_F rather appears to be the consequence of a Peierls distortion along the Co···Co chains. Accordingly, the electronic band structure of HT-**2** along a *k*-point path parallel to the chains (Figure 4) shows the prototypical electronic signatures of a 1D atomic chain. The states originating from the d_{z^2} type orbitals orientated along the Co···Co chains direction split into two branches with a large energetic gap at Γ and a small splitting due to a symmetry based avoided crossing at $k = \pm ½, 0, 0$ (*k* defined with respect to the reciprocal conventional vec-

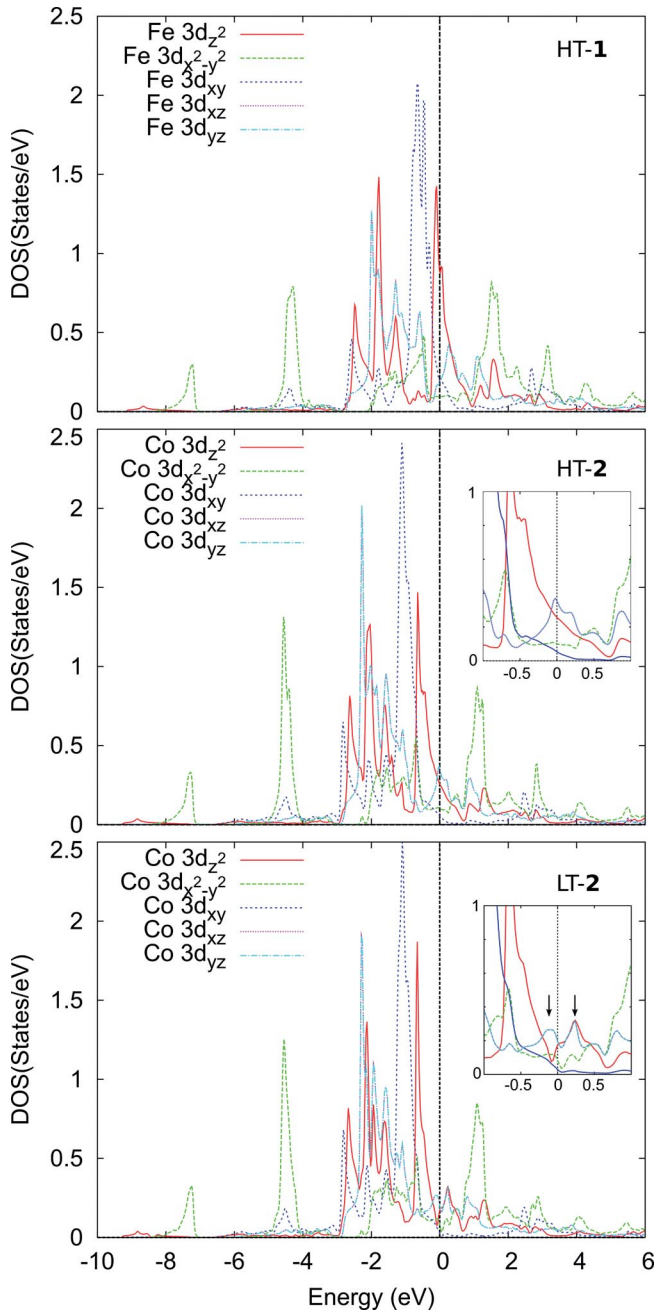

Figure 3. Site- and state projected density of states (pDOS in states/eV and atom) for HT-**1**, HT-**2**, and LT-**2** in the energy range between –10 and 6 eV. The position of the Fermi level (E_F) is indicated by a dashed line, the arrows mark the changes to the pDOS at E_F

Zeitschrift für anorganische und allgemeine Chemie ZAAC Journal of Inorganic and General Chemistry

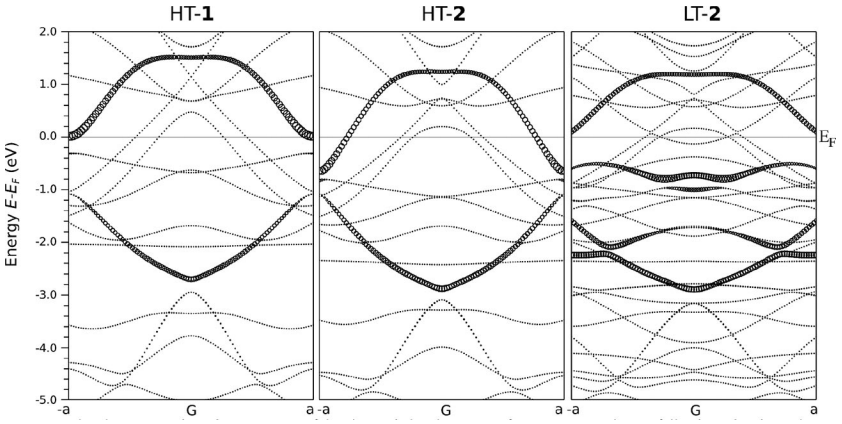

Figure 4. Fat-band representation (d_{z^2}-type states) of the electronic bandstructure of HT-**1**, HT-**2**, and LT-**2** following a *k*-point path perpendicular to the direction of the $[T(C_2)_2]$ ribbons (for the definitions of the paths, see the Supporting Information).

tors, for details see the Supporting Information). Comparing the according bandstructures of HT-**1** and HT-**2** (Figure 4), two main differences emerge. We first note the different position of E_F with respect to the bonding and non-bonding bands established by the d_{z^2} type states. In case of the d^8-configured Fe carbide (HT-**1**) the non-bonding d_{z^2} type states are situated above E_F (Figure 4). The non-bonding character of the d_{z^2} type states in HT-**1** is also warranted by the larger splitting of the d_{z^2} type states in the HT-**1** versus HT-**2** phase. As a consequence, at $k = \pm ½, 0, 0$ all non-bonding states are unoccupied. In contrast to this, due to the increasing electron count of HT-**2** (containing a d^9-configured Co atom), these non-bonding states are partially filled (ca. 0.42 e^- derived from the d_{z^2} pDOS).[20] This scenario of unevenly occupied, degenerate states is the prerequisite to initiate a Peierls distortion in a 1D chain of equidistant atoms. In accordance with this, the band structure of LT-**2** shows the opening of a gap in the d_{z^2} type states at E_F and an energetic lowering of the bonding branch formed by the d_{z^2} type states. Hence, the occupied bonding and partially occupied non-bonding bands of d_{z^2}-type character in HT-**2** split into three (occupied) bonding and one (unoccupied) non-bonding band in LT-**2**. In real space we observe the respective doubling of the unit cell volume, which accounts for the increase of the number of bands by a factor of 2. The non-bonding branch now resides completely above E_F as in the case of HT-**1**. Therefore, the driving force of the structural phase transition in **2** can clearly be identified to be a Peierls distortion and discriminated from the electronic situation in **1**, which appears to be inert to such a distortion due to the lacking electronic prerequisites. We further note, that the splitting of the $d_{xz/yz}$ states in LT-**2** at E_F as a consequence of this Peierls transition also involves an additional π-type contribution to the Co–Co bonding in LT-**2**. The latter contribution together with the strengthening of the Co–Co σ-type interaction appears to be the chemical driving force of this process.

In the last step of our electronic structure analysis we will focus on real space properties of the electron density distribution in **1** and **2**. We first attempt to trace the origin of the asymmetric $L(\mathbf{r})$ pattern displayed by the cobalt atoms along the 1D $[Co\cdots Co]_n$ chains in LT-**2** (Figure 2e) by a band structure analysis. Figure 5 depicts the p_z fat-band representation of the band structure of HT-**2** and LT-**2** along the same *k* path as employed in Figure 4. In the HT phase, the site symmetry of the cobalt atoms is D_{2h} at the gamma (Γ) point, $k = 0,0,0$. Hence, the d_{z^2} and p_z orbitals transform as a_g and b_{1u} irreps at this k-point, respectively, and hybridization of these orbitals is prevented for symmetry reasons. Accordingly, no mixing of the p_z states into the d_{z^2} states can be observed at the gamma point (see Figure 2d above). In contrast, the site symmetry at $k = \Gamma$ is reduced to C_s in case of the LT phase. Using the local coordinate system as defined above and employed throughout our study the p_z and d_{z^2} orbitals transform as irrep a'. Hence, hybridization of these orbitals can occur in the low temperature phase what is clearly revealed in the fat-band representations of Figure 5. The mixing of the d- and p-states thus results in the formation of metal centered hybrid orbitals with asymmetric orbital lobes along the Co···Co chain direction (see Figure 2f) were the larger lobes of two neighboring cobalt atoms (resulting from the constructive overlap between the p_z- and d_{z^2}-type orbital) are opposing each other in the bonding region

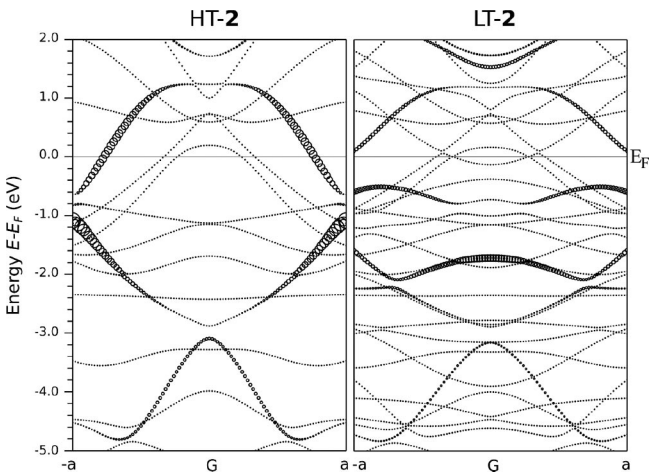

Figure 5. Fat-band representation (p_z-type states) of the electronic bandstructure of HT-**2** and LT-**2** along the same *k*-point path as defined in Figure 4.

marked by the short Co···Co contact. Therefore, the hybridization of the p and d orbitals leads to an increase/decrease of the orbital overlap in the bonding region of the short/long Co···Co contacts. This result underpins nicely the close resemblance of the orbital and the charge density picture yielding the same bonding description for the alternating short and long Co···Co contacts. Hence, the topology of the charge density and the crystal orbitals are linked with each other as "two sides of the same coin".

In summary, the establishment of alternating {···Co–Co···Co–Co}$_n$ chains perpendicular to the quasi one-dimensional [T(C$_2$)$_2$]-ribbons is a natural consequence of a Peierls distortion during the HT-**2** → LT-**2** phase transition. Hence, the low-temperature phase of Sc_3CoC_4 displays two structural moieties of quasi one-dimensional character. Since the iron carbide Sc_3FeC_4 does not display any Peierls-type transition we presume already at this stage, that the onset of superconductivity in the Co carbide is strongly connected with the presence of the alternating {···Co–Co···Co–Co}$_n$ chains. To get a more definite answer we will therefore investigate in the next step of our analysis the phonon spectra of both carbides **1** and **2**.

Vibrational Properties

A Peierls-type structural transition requires the presence of an appropriate vibrational mode of suitable symmetry to drive the distortion. We therefore analysed the changes of the phonon-spectra as a consequence of the HT → LT phase transition of **2**. Figure 6 depicts the phonon dispersion relation together with the site-projected phononic DOS (pPDOS) of both phases. We identify four well separated frequency ranges for the optical branches of the phonon dispersion curves. These regions can to a large extend be attributed to the different atom types involved in the according vibrations. The lowest lying modes (below 10 THz) are dominated by Sc and Co contributions, while the modes between 10 and 17 THz are already largely dominated by the vibrations involving the lighter carbon atoms and only to a lesser degree by contributions from the Co atoms. The two branches between 17–20 and 28–32 THz are solely due to the motion of the carbon atoms. We note that the according geometry relaxations for the iron congener **1** did not result in vibrationally stable ground state geometry if the iron atom was placed at the cobalt position in the LT-phase of **2**. This finding is in accordance with the experimentally observed fact that the HT → LT phase transition observed for **2** has not yet been observed for **1** and seems to be energetically disfavored down to temperatures of 2 K.

The major differences between the phononic spectra of HT-**2** and LT-**2** can be traced to the occurrence of a relatively sharp maximum in the pPDOS of HT-**2** at approx. 4 THz, indicating a soft mode characterized by a rather low dispersion. Analysis of the phononic band structure of HT-**2** reveals that this pPDOS peak originates from a softening of the longitudinal acoustic (LA) mode in comparison with the respective transversal acoustic (TA) modes. The frequency of the LA mode features a local minimum when we consider again the k path

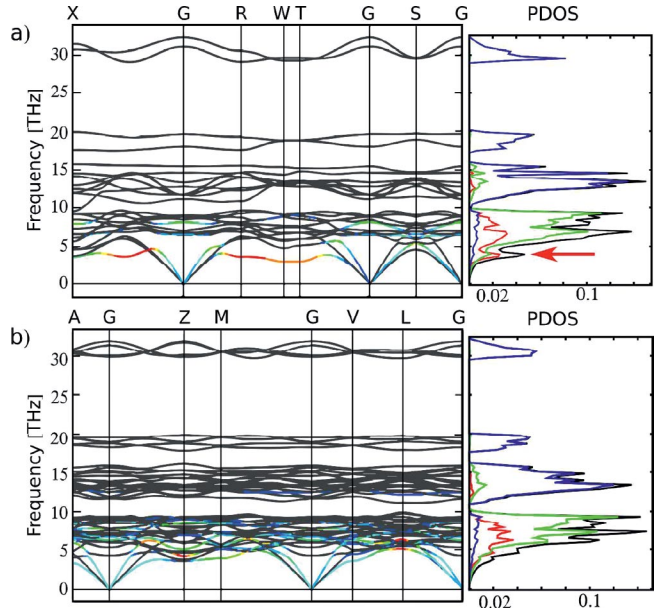

Figure 6. Phononic bandstructure and total/site-projected vibrational density of states of (a) HT-**2** and (b) LT-**2**. In the dispersion curves, the colors decode the Co atom displacement contributions (black zero, blue low, and red high values) in direction of the crystallographic *a* axis and *a,b* diagonal for HT-**2** and LT-**2**, respectively. In the pPDOS representation, the total PDOS is drawn as a black line, the contributions of the carbon, scandium and cobalt atoms as blue, green, and red lines, respectively. The position of the peak in the PDOS resulting from the soft LA mode in HT-**2** (see text) is indicated by a red arrow.

Γ → (½, 0, 0), which might hint for the presence of a Kohn anomaly.[21] The latter phenomenon would provide further support of the quasi-1D character of Sc_3CoC_4 and explain its instability with respect to charge-density wave formation or a Peierls-type distortion.[21] At q = (½, ½, 0) this mode (ω = 3.032 THz) displays exactly the required symmetry to drive the Peierls transition discussed above (see Scheme 2). In case of the distorted LT-**2** phase the corresponding mode showing the same atomic displacements as in HT-**2** occurs as a soft optical mode with ω = 4.224 THz at the Γ point. This yields an energetic difference of 0.48 kJ·mol^{-1}, in agreement with the identification of the strengthening of the Co–Co interaction as the chemical driving force of the phase transition.

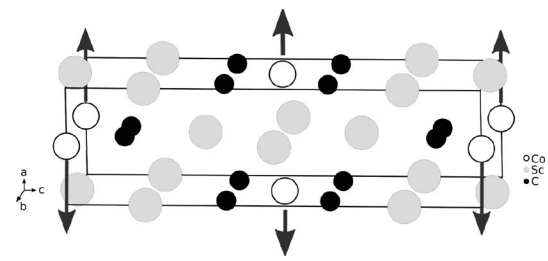

Scheme 2. Schematic representation of the atomic displacements of the LA mode of HT-**2** at k = ½, ½, 0. The arrows indicate the direction of the displacements of the Co atoms, which represent the dominant contribution to the overall atomic movement of the according vibrational mode.

Zeitschrift für anorganische und allgemeine Chemie ZAAC Journal of Inorganic and General Chemistry

The Solid Solution $Sc_3Co_{1-x}Fe_xC_4$

Interpretation of the electronic and phononic band structure clearly identified the gap opening at E_F as electronic driving force for the HT → LT phase transition in **2**. The splitting of the d_{z^2} pDOS peak into bonding and non-bonding states initiates the Peierls-type distortion and enhances the Co–Co interactions. This result suggests that the phase transition will be suppressed if the nonbonding d_{z^2} states (occupied by approx. 0.42 electrons per Co atom) become depopulated in the HT-**2** phase by performing a partial substitution of the Co atoms by Fe. Such substitution should cause a lowering of E_F and the transition will be supressed when E_F reaches the level of the gap between the bonding and non-bonding branches of the d_{z^2} type states of LT-**2** (Figure 4) at the edge of the Brillouin zone.

We therefore synthesized the solid solutions $Sc_3Co_{1-x}Fe_xC_4$ (x = 0.05, 0.1, 0.2, 0.3, 0.5, 0.75) and $Sc_3Co_{1-x}Ni_xC_4$ (x = 0.05, 0.1) in order to study the effect of a change of the valence electron count on the electronic and structural properties of **2**. Figure 7 depicts the change in the lattice parameters for both series as obtained from Rietveld refinements. The solid solutions (Sc_3FeC_4 → Sc_3CoC_4 → Sc_3NiC_4) obey Vegard's law and the length of the crystallographic a and c axes increase (+1.3 %) and decrease (–1.5 %) linearly, respectively. In contrast, the b axis shows a V-shaped dependency on x. It shrinks linearly (overall by 0.2 %) due to the substitution of Fe by Co and increases again (overall by 0.4 %) when replacing Co by Ni. Considering the resulting unit cell volumes, again a V-shaped pattern is observed, the cell of HT-**2** being 0.4 % smaller than the unit cell of the start and end members of the solid solution (Sc_3FeC_4 and Sc_3NiC_4), which in turn show remarkably similar cell volumes.

We can correlate these structural parameters directly with the length of the *T*···*T* contacts in and perpendicular to the [$T(C_2)_2$] ribbon direction since the a axis is oriented parallel to the *T*–*T* bonding vector, while the b axis parallels the *T*–*T* directions inside the [$T(C_2)_2$] ribbons. We note that the a lattice parameter controls the *T*···*T* contacts perpendicular to the [$T(C_2)_2$] ribbons and would therefore be directly affected by a potential effect of the substitution of the metal atom on this interaction. We note that the small but significant linear increase of the a lattice parameter upon stepwise substitution of Fe by Co and Ni in these solid solutions counteracts the decreasing ionic/atomic radii along the series of these Group 8–10 elements. This observation therefore supports our suggestion, that the strength of the *T*···*T* interactions is mainly controlled by the d electron count of the metal. Accordingly, *T*···*T* bonding is pronounced for *T* = Fe already in the HT phase while for *T* = Ni featuring an almost completely filled d^{10} shell no energetic stabilization due to the *T*···*T* interaction is expected. Hence, the Nickel species lacks any energetic motivation to optimize these *T*···*T* interaction via the structural HT → LT phase transition (in contrast to its Co analogue). Therefore we may assume, that the general electronic structure of the systems remains intact so that any change observed for the HT → LT transition for the solid solutions of **2** appears to be solely controlled by the population of the nonbonding

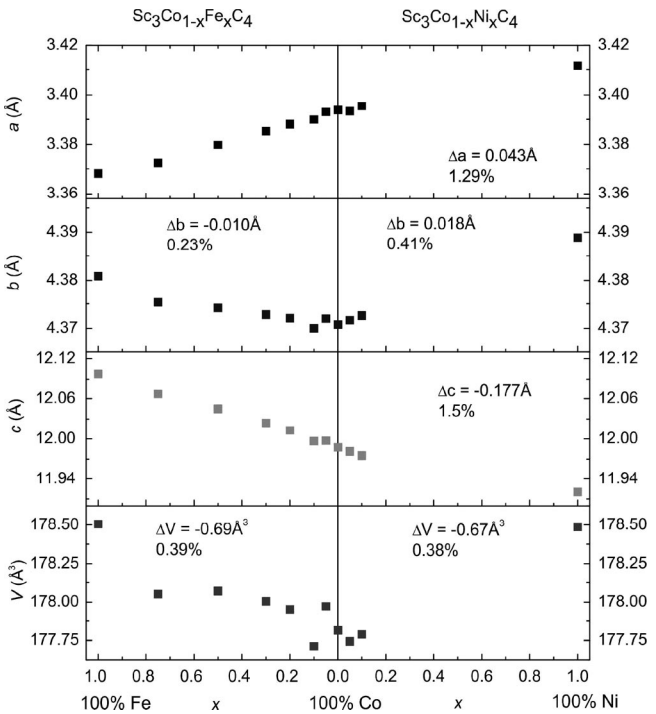

Figure 7. Change of the lattice parameters a, b, c and the unit cell volume V in the solid solution $Sc_3Co_{1-x}Fe_xC_4$ (x = 0, 0.05, 0.1, 0.2, 0.3) and $Sc_3Co_{1-x}Ni_xC_4$ (x = 0.05, 0.1) as obtained from Rietveld refinements of powder X-ray diffraction data.

d_{z^2} states at E_F and thus by the valence electron count – in agreement with our band structure analysis.

In order to investigate the differences in the physical and structural properties, we measured the molar susceptibility and the specific resistivity of these solid solutions (see Figure 8) in a temperature range $2 < T < 300$ K. As shown before, the susceptibility data of the parent compound **2** hint for the occurrence of a charge density wave at approx. 140 K, while the sudden drop of $\chi(T)$ at 72 K can be correlated to the phase transition from HT- to LT-**2**.[4] The latter anomaly is accompanied by a non-reversible transition in the specific resistivity data. This is most likely caused by the stress induced by the systematic twinning of the sample during the structural phase transition.[1]

In direct comparison with the parent system $Sc_3Co_{1-x}T_xC_4$ (T = Fe, Ni; x = 0.0), already minute changes of the sample composition (x = 0.05) yield a distinct different physical behavior. In the latter case, the $\chi(T)$ susceptibility data show for T = Fe only one broad transition centered at approx. 100 K, which is (as in the parent compound **2**) accompanied by the onset of a non-reversible transition in the resistivity data. From this observation we conclude, that the structural phase transition has shifted from T_s = 72 K in **2** to approx. 100 K in $Sc_3Co_{1-x}Fe_xC_4$ (x = 0.05). Increasing the iron content further from x = 0.05 to x = 0.1 and 0.2 (which corresponds to a further depopulation of the nonbonding d_{z^2}-states at E_F), shifts the transition temperature T_s to even higher values (107 K and approx. 125 K, respectively). For $x > 0.3$ (Figure 8) the phase transition becomes finally suppressed and the $\chi(T)$ suscep-

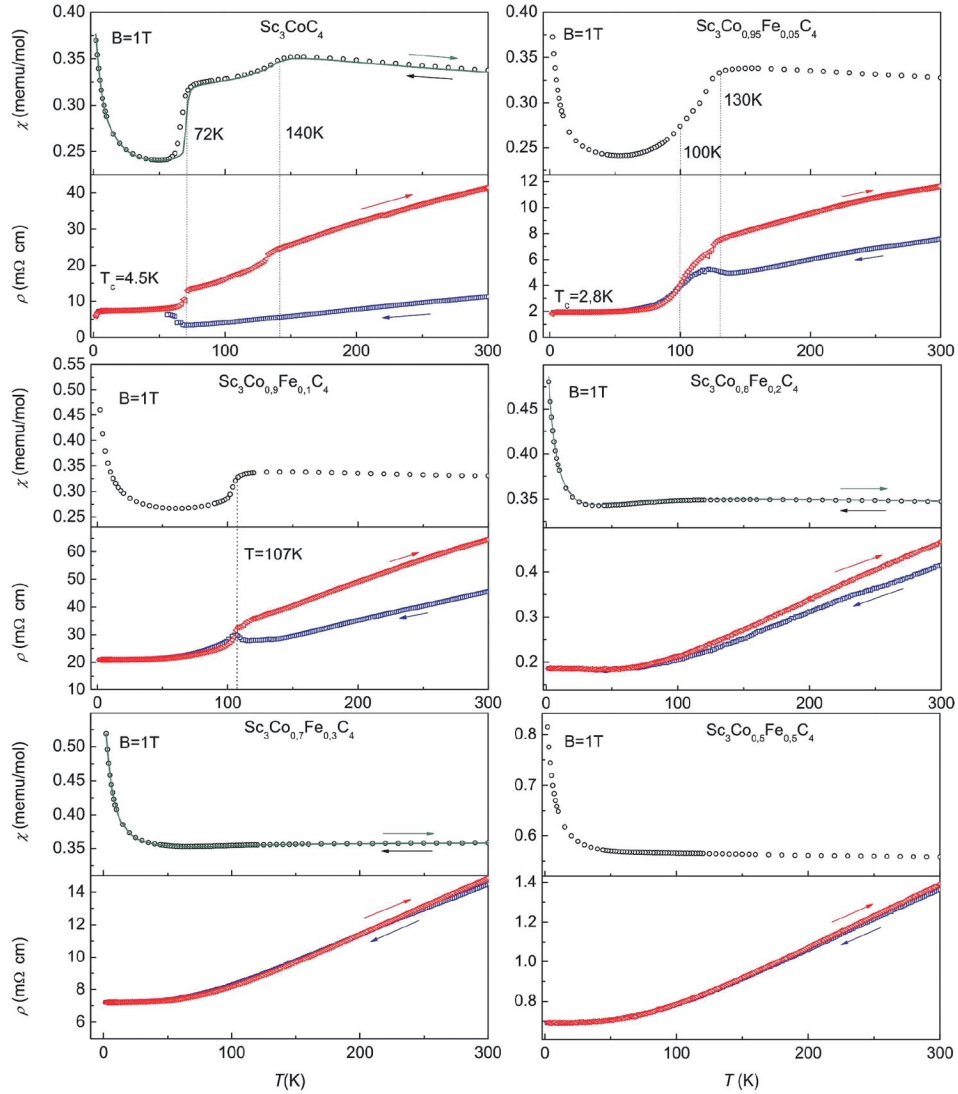

Figure 8. Temperature dependence of the molar susceptibility $\chi(T)$ and the specific resistivity $\rho(T)$ of the solid solution $Sc_3Co_{1-x}Fe_xC_4$ (x = 0, 0.05, 0.1, 0.2, 0.3, 0.5) in the temperature range 2 K $< T <$ 300 K.

tibility as well as the $\rho(T)$ resistivity curves indicate a normal metallic behavior of the sample. With the shift of T_s to higher temperatures, the superconducting transition which was observed at T_c = 4.5 K for **2** becomes reduced to T_c = 2.8 K for x = 0.05. For even higher iron concentrations no superconducting transition could be observed in the temperature range covered within the presented study (>2 K). The above results of the solid solution $Sc_3Co_{1-x}Fe_xC_4$ together with those obtained for $Sc_3Co_{0.95}Ni_{0.05}C_4$ are summarized in a phase diagram (Figure 9), which illustrates how the increasing iron and nickel content shifts the structural phase transition to higher temperatures and finally suppresses the Peierls transition for T = Fe at $x > 0.3$ and T = Ni at $x > 0.05$, respectively. This behavior coincides with a lowering of T_c and finally the suppression of the onset of superconductivity. This clearly underpins the linkage of the structural phase transition and the onset of superconductivity in **2**. The results also confirm our prediction from the band structure analysis: The Peierls transition is controlled by the presence of nonbonding d_{z^2}-type states at the Fermi energy, which can be chemically controlled by the valence electron count at the transition metal in the $[T(C_2)_2]$-ribbons.

Conclusions

To conclude, the establishment of alternating {···Co–Co···Co–Co}$_n$ chains perpendicular to the quasi one-dimensional $[T(C_2)_2]$-ribbons is a natural consequence of the Peierls distortion during the HT-**2** → LT-**2** phase transition. The Peierls transition itself is initiated by the presence of nonbonding d_{z^2} type states at the Fermi energy. The splitting of the d_{z^2} pDOS peak (occupied by approx. 0.42 electrons) into bonding and non-bonding states initiates the Peierls-type distortion and enhanced the Co–Co interactions. Hence, the transition can be

Zeitschrift für anorganische und allgemeine Chemie ZAAC Journal of Inorganic and General Chemistry

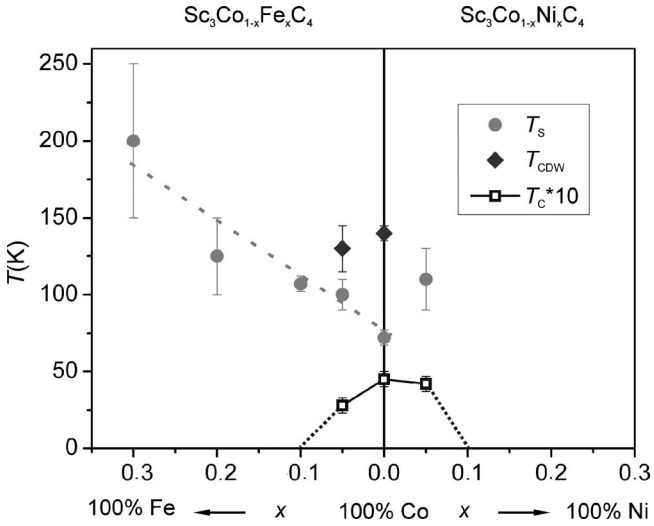

Figure 9. Preliminary phase diagram derived for the solid solutions $Sc_3Co_{1-x}Fe_xC_4$ (x = 0.0, 0.05, 0.1, 0.2, 0.3, 0.5, 0.75) and $Sc_3Co_{1-x}Ni_xC_4$ (x = 0.05, 0.1) indicating the temperature vs. x dependency of the structural phase transition (T_s), the onset of superconductivity (T_c) and the formation of a charge density wave (T_{CDW}) (see Ref. [4]).

chemically controlled by the valence electron count at the transition metal in the $[T(C_2)_2]$-ribbons.

We further point out, that the electronic instability of the equidistant $\{Co–Co–Co\}_n$ chains of HT-**2** at low temperatures is corroborated by a softening of the according longitudinal optical vibrational mode driving the Peierls distortion. We finally note, that the onset of superconductivity in the cobalt carbide is strongly connected with the formation of the alternating $\{\cdots Co–Co\cdots Co–Co\}_n$ chains perpendicular to the $[T(C_2)_2]$ ribbons.

Experimental Section

Sample Preparation: Samples of **2** were prepared according to literature methods from the elements.[8] For the solid solution $Sc_3Co_{1-x}Fe_xC_4$, samples were prepared from the elements (purities > 99.9 %) by reaction of mixtures of the according atomic ratios in a standard arc melting furnace. The product buttons were remelted four times to ensure sample homogeneity, the total weight losses after the procedure were smaller than 0.8 % for x = 0.05 and smaller than 0.5 % in all other cases. The stoichiometry of the samples was verified by ICP-OES measurements and the phase purity of the samples was checked by X-ray powder diffraction.

Neutron Powder Diffraction Experiments: Variable temperature (VT) neutron powder diffraction data was collected with cold neutrons (λ = 2.423 Å) with the two-axis diffractometer G4–1 of the LLB-Orphée reactor (Saclay). Data was recorded in the range $3° < 2\theta < 82.9°$ with a step-width of 0.1°.

Neutron powder diffraction data was also collected with thermal neutrons (Ge monochromated, λ = 1.225 Å) at the high-resolution two-axis diffractometer at the 3T2 beamline of the LLB-Orphée reactor (Saclay) at variable temperatures (160 K, 100 K and 10 K). Data was recorded employing the ^{3}He detector array in the range $4.5° < 2\theta < 121°$ with a step-width of 0.05°.

Single Crystal X-ray Diffraction at 8 K on LT-2

Data Collection: A black block-like crystal of **2** with dimensions $0.021 \times 0.038 \times 0.092$ mm^3 was selected and mounted on top of a MiTeGen MicroMount using perfluorinated polyether, which was mounted in an open-flow helium stream (Helijet, Oxford Diffraction) at 8(2) K with a SMART APEX2 fixed-χ goniometer (Bruker). The data collection was carried out using a IμS micro-focus sealed tube (Ag-K_α; λ = 0.56087 Å) equipped with a Montel multilayer-optic (Incoatec). Intensity data were collected with a Bruker APEX II CCD-detector.

Data Reduction and Refinement: Due to the systematically pseudo-merohedrically twinned crystal an empirical absorption correction was applied using the program TWINABS (T_{min} = 0.470, T_{max} = 1.000) for a total of 6402 reflections (2161/2145 single and 2096 composite reflections) yielding 1486 unique reflections [$R_{int}(F^2)$ = 0.0655, 97.1 % completeness for $5.36° < 2\theta < 68.20°$].[22] For the refinements a HKLF5 formatted data file with 2702 reflections was used.

A combined refinements of the neutron powder- and single crystal data was performed employing the crystallographic software package JANA2006.[23] The already published low temperature structure of Sc_3CoC_4 was used as a starting model.[4] For further information see Supporting Information.

Charge Density Study on Sc_3CoC_4 (HT-2)

Data Collection: A metallic gray cuboid shaped crystal of Sc_3CoC_4 with the dimensions $0.04 \times 0.05 \times 0.08$ mm^3 was gained by cutting a whisker, obtained directly from the synthesis, and mounted on top of a MiTeGen MicroMount using perflourinated polyether, which was fixed on a SMART APEX2 fixed-χ goniometer (Bruker) at room temperature. The data collection was carried out using a IμS micro-focus sealed tube (Ag-K_α; λ = 0.56087 Å) equipped with a Montel multilayer-optic (Incoatec). Intensity data were collected with a Bruker APEX II CCD-detector and 0.5° ω- and ϕ-scans with a detector-to-sample distance of 40 mm.

Crystal Data for HT-2: M_r = 241.85, orthorhombic, space group *Immm*, a = 3.39483(3), b = 4.37484(4), c = 11.9971(1) Å, V = 178.179(3) Å^3; Z = 2, $F(000)$ = 228, D_{calc} = 4.508 g·cm^{-3}, μ = 5.01 mm^{-1}. A numerical absorption correction was applied (T_{min} = 0.764, T_{max} = 0.830) with the program SADABS.[24] The internal agreement factor was $R_{int}(F^2)$ = 0.0355 for a total of 23618 reflections yielding 1176 unique reflections. This data set provided 100 % completeness in $2° < 2\theta < 102.4°$ ($\sin\theta_{max}/\lambda < 1.389$ Å^{-1}).

The deformation density was described by a multipolar model in terms of spherical harmonics multiplied by Slater-type radial functions with energy-optimised exponents.[25,26,27] The refinement of 56 parameters against 989 observed reflections [$F_o > 3\sigma(F)$, $\sin\theta_{max}/\lambda$ = 1.322 Å^{-1}] converged to R_1 = 0.0091, wR_2 = 0.0217, and a featureless residual density map with minimum and maximum values of 0.219/–0.207 e·Å^{-3}. For further information see Supporting Information.

DFT Calculations

Geometry relaxation calculations were performed for **1** and **2** employing VASP.[28–31] The PBE functional was used throughout,[32,33] with 520 eV for the energy cutoff and a Brillouin grid sampling of $4 \times 4 \times 2$ for the HT structure and $2 \times 2 \times 2$ for the LT case. Force convergence was checked for the chosen parameters to be less than

Special Issue

0.01 eV/A. PAW pseudopotentials were used to describe non-valence electrons. Electronic structure calculations on these relaxed geometries were performed employing the Wien2k suite of programs using an augmented plane wave basis set with additional local orbitals (APW+lo).[34] For the SCF cycle, a set of 512 (816 for LT-**2**) irreducible k-points for the sampling of the Brillouin zone was used. The site and state projected density of states and band character plots were calculated employing a rotated reference coordinate system described in the Supporting Information and in Ref. [3]. The analysis of the topology of the electron density obtained from the Wien2k calculations was performed employing the program CRITIC.[35] Local maxima in the Laplacian of the electron density were determined graphically using the VMD software.[36]

Phonon calculations on **1** and **2** were performed on the ground state geometries obtained from the previous relaxation runs employing the PHONON program.[37,38] A $2\times2\times2$ supercell was constructed, in which displacements of 0.03 Å were introduced for the force calculations performed employing the VASP program.

Supporting Information (see footnote on the first page of this article): Tables of crystallographic data, details of the VT neutron powder diffraction experiments, details of the multipolar refinements, atomic coordinates, anisotropic thermal parameters and residual electron density maps, specifications of the local coordinate systems employed, multipol population parameters for **2**, definitions of the k-point paths, details on the electronic structure calculations, temperature dependence of the molecular susceptibility and the specific resistivity of the solid solutions $Sc_3Co_{1-x}Ni_xC_4$ (x = 0.05, 1) and $Sc_3Co_{1-x}Fe_xC4$ (x = 0.75).

Note added in proof: In a recent contribution published by *Zhang* et al. the authors quote our experimental results (Ref. [4]) for the wrong reasons: "Even more surprisingly, a superconducting phase was found at below 4.5 K and attributed to the charge density wave-like (CDW) distortion. The coexistence of CDW and superconductivity is unusual and this suggestion motivated the present study."[39] This is in clear conflict with our earlier findings, where we clearly stated that "This result might provide first evidence that the superconducting transition below 4.5 K in Sc_3CoC_4 critically depends on the presence of a Peierls-type transition along the transition-metal chains. This suggestion is further supported by the change in electrical resistivity [of Sc_3CoC_4] on cooling, which reveals a distinct increase of the ρ(T) values below the structural transition temperature at 72 K."

We further note, that the electronic structure of Sc_3CoC_4 cannot be interpreted in terms of the Zintl-Klemm concept as suggested by *Zhang* et al.[39] Such interpretation is in clear conflict with our experimental and electronic structure analyses as reported in this contribution and in earlier publications (Refs. [1,3,4]).

We finally remark that also the following statement of the latter authors is highly misleading and at odds with our experimental reports: "*It has been revealed that the nature of electron-phonon superconductivity can be intrinsic to Sc_3CoC_4 and exist even in the high-pressure orthorhombic structure*."[39] By a more careful study of our published experimental results, *Zhang* et al. might have noticed, that the orthorhombic phase which occurs above 72 K (Ref. [4]) actually represents the high-temperature modification of Sc_3CoC_4 which – so far – did not show any onset of superconductivity.

Acknowledgements

This work was supported by the Deutsche Forschungsgemeinschaft (DFG) within the special priority program SPP1178, AHR acknowledges the support from Marie-Curie Intra-European Fellowship, AM was supported by the Spanish National Program of Materials (MAT2010–21270-C04/03).

References

[1] W. Scherer, G. Eickerling, C. Hauf, M. Presnitz, E.-W. Scheidt, V. Eyert, R. Pöttgen, in *Modern Charge-Density Analysis* (Eds.: C. Gatti, P. Macchi), Springer, Netherlands **2012**, pp. 359–385.
[2] R. Hoffmann, J. Li, R. A. Wheeler, *J. Am. Chem. Soc.* **1987**, *109*, 6600–6602.
[3] B. Rohrmoser, G. Eickerling, M. Presnitz, W. Scherer, V. Eyert, R. D. Hoffmann, U. C. Rodewald, C. Vogt, R. Pöttgen, *J. Am. Chem. Soc.* **2007**, *129*, 9356–9365.
[4] W. Scherer, C. Hauf, M. Presnitz, E.-W. Scheidt, G. Eickerling, V. Eyert, R.-D. Hoffmann, U. C. Rodewald, A. Hammerschmidt, C. Vogt, R. Pöttgen, *Angew. Chem. Int. Ed.* **2010**, *49*, 1578–1582.
[5] E.-W. Scheidt, C. Hauf, F. Reiner, G. Eickerling, W. Scherer, *J. Phys. Conf. Ser.* **2011**, *273*, 012083.
[6] M. He, D. Shi, P. L. Tse, C. H. Wong, O. Wybranski, E.-W. Scheidt, G. Eickerling, W. Scherer, P. Sheng, R. Lortz, *arXiv:1211.5430*.
[7] J. Bardeen, L. N. Cooper, J. R. Schrieffer, *Phys. Rev.* **1957**, *108*, 1175–1204.
[8] C. Vogt, R.-D. Hoffmann, U. Ch. Rodewald, G. Eickerling, M. Presnitz, V. Eyert, W. Scherer, R. Pöttgen, *Inorg. Chem.* **2009**, *48*, 6436–6451.
[9] P. M. Morse, H. Feshbach, *Methods of Theoretical Physics*, McGraw-Hill, **1953**.
[10] R. F. W. Bader, P. J. MacDougall, C. D. H. Lau, *J. Am. Chem. Soc.* **1984**, *106*, 1594–1605.
[11] R. F. W. Bader, P. M. Beddall, *J. Chem. Phys.* **1972**, *56*, 3320–3329.
[12] R. F. W. Bader, H. Essén, *J. Chem. Phys.* **1984**, *80*, 1943–1960.
[13] R. P. Sagar, A. C. T. Ku, V. H. Smith, A. M. Simas, *J. Chem. Phys.* **1988**, *88*, 4367–4374.
[14] Z. Shi, R. J. Boyd, *J. Chem. Phys.* **1988**, *88*, 4375–4377.
[15] W.-T. Chan, I. P. Hamilton, *J. Chem. Phys.* **1998**, *108*, 2473–2485.
[16] Furthermore, four-component calculations on spherical symmetric atoms (Au) by *Kohout* et al. showed that the outermost shell of elements of period 6 might not be resolved in the second dericative of the radial density: M. Kohout, A. Savin, H. Preuss, *J. Chem. Phys.* **1991**, *95*, 1928–1942. For further information, see: G. Eickerling, M. Reiher, *J. Chem. Theory Comput.* **2008**, *4*, 286–296; N. Hebben, H.-J. Himmel, G. Eickerling, C. Herrmann, M. Reiher, V. Herz, M. Presnitz, W. Scherer, *Chem. Eur. J.* **2007**, *13*, 10078–10087; and Ref. [8].
[17] R. F. W. Bader, R. J. Gillespie, F. Martin, *Chem. Phys. Lett.* **1998**, *290*, 488–494.
[18] G. S. McGrady, A. Haaland, H. P. Verne, H. V. Volden, A. J. Downs, D. Shorokhov, G. Eickerling, W. Scherer, *Chem. Eur. J.* **2005**, *11*, 4921–4934.
[19] The $d_{xy/xz}$ orbitals belong to the irreducible representation (irrep) E_g if we assume the highest possible site symmetry of D_{4h} for the cobalt atoms in the $[TM(C_2)_2]$ ribbons. Reducing the symmetry to D_{2h} (HT-**2**) and further to C_s (LT-**2**) causes a lifting of the energetic degeneracy of these orbitals yielding the states of b_{2g}/b_{3g} symmetry in case of HT-**2** and two states of a'' symmetry in LT-**2**. Accordingly, the HT to LT phase transition could be formally classified as a second order Jahn-Teller effect since the degeneracy of the cobalt d-orbitals was already lifted in the HT-**2** phase.
[20] This value was derived from the d_{z^2} pDOS contributions inside the cobalt atom's muffin tin spheres only. The states in the interstitial part outside the muffin tin spheres which within the LAPW ansatz is modeled by a plane-wave basis set cannot be projected onto specific sites or states and must thus be neglected for this analysis.

[21] G. Grüner, *Density Waves In Solids*, Addison-Wesley, Reading, Mass. u. a., **1994**, p. 32ff.
[22] G. M. Sheldrick, *TWINABS* – Bruker *AXS*, Scaling for Twinned Crystals, Göttingen, Germany, **2008**.
[23] V. Petricek, M. Dusek, L. Palatinus, *Jana2006*, The Crystallographic Computing System, Praha, Czech Republic, **2006**.
[24] G. M. Sheldrick, *SADABS*, Göttingen, Germany, **2008**.
[25] A. Volkov, P. Macchi, L. J. Farrugia, C. Gatti, P. Mallinson, T. Richter, T. Koritsanszky, XD2006 (v. 5.42) – A Computer Program for Multipol Refinement, Topological Analysis of Charge Densities and Evaluation of Intermolecular Energies from Experimental and Theoretical Structure Factors, **2006**.
[26] Z. Su, P. Coppens, *Acta Crystallogr., Sect. A* **1998**, *54*, 646–652.
[27] E. Clementi, D. L. Raimondi, *J. Chem. Phys.* **1963**, *38*, 2686–2689.
[28] G. Kresse, J. Hafner, *Phys. Rev. B* **1993**, *47*, 558–561.
[29] G. Kresse, J. Furthmüller, *Phys. Rev. B* **1996**, *54*, 11169–11186.
[30] G. Kresse, J. Hafner, *Phys. Rev. B* **1994**, *49*, 14251–14269.
[31] G. Kresse, J. Furthmüller, *Comput. Mater. Sci.* **1996**, *6*, 15–50.
[32] J. P. Perdew, K. Burke, M. Ernzerhof, *Phys. Rev. Lett.* **1996**, *77*, 3865–3868.
[33] J. P. Perdew, K. Burke, M. Ernzerhof, *Phys. Rev. Lett.* **1997**, *78*, 1396.
[34] P. Blaha, K. Schwarz, G. K. H. Madsen, D. Kvasnicka, J. Luitz, *WIEN2k*, An Augmented Plane Wave + Local Orbitals Program for Calculating Crystal Properties, Technische Universität Wien, Wien, Austria, **2001**.
[35] A. Otero-de-la-Roza, M. A. Blanco, A. M. Pendás, V. Luaña, *Comput. Phys. Commun.* **2009**, *180*, 157–166.
[36] W. Humphrey, A. Dalke, K. Schulten, *J. Mol. Graphics* **1996**, *14*, 33–38.
[37] K. Parlinski, *Phonon*, Cracow, **2010**.
[38] K. Parlinski, Z. Q. Li, Y. Kawazoe, *Phys. Rev. Lett.* **1997**, *78*, 4063–4066.
[39] C. Zhang, J. S. Tse, K. Tanaka, H.-Q. Lin, *EPL* **2012**, *100*, 67003.

Received: November 27, 2012
Published Online: June 24, 2013

Special Issue

